

## An XUV-FEL amplifier seeded using high harmonic generation

**B W J McNeil<sup>1,5</sup>, J A Clarke<sup>2</sup>, D J Dunning<sup>2</sup>, G J Hirst<sup>3</sup>,  
H L Owen<sup>2</sup>, N R Thompson<sup>2</sup>, B Sheehy<sup>4</sup> and P H Williams<sup>2</sup>**

<sup>1</sup> Scottish Universities Physics Alliance, Department of Physics,  
University of Strathclyde, Glasgow, UK

<sup>2</sup> Accelerator Science and Technology Centre, CCLRC Daresbury Laboratory,  
Daresbury, UK

<sup>3</sup> Central Laser Facility, CCLRC Rutherford Appleton Laboratory, Didcot, UK

<sup>4</sup> Sheehy Scientific Consulting, New York, USA

E-mail: [b.w.j.mcneil@strath.ac.uk](mailto:b.w.j.mcneil@strath.ac.uk)

*New Journal of Physics* **9** (2007) 82

Received 5 January 2007

Published 3 April 2007

Online at <http://www.njp.org/>

doi:10.1088/1367-2630/9/4/082

**Abstract.** A detailed design of a free electron laser (FEL) amplifier operating in the extreme ultra violet (XUV) and seeded directly by a high harmonic source is presented. The design is part of the 4th generation light source (4GLS) facility proposed for the Daresbury Laboratory in the UK which will offer users a suite of high brightness synchronised sources from THz frequencies into the XUV. The XUV-FEL will generate photons with tunable energies from 8 to 100 eV at giga-watt peak power levels in near Fourier-transform limited pulses of variable polarisation. The designs of the high harmonic generation (HHG) seeding, FEL amplifier and synchronising systems are presented. Numerical simulations quantify the FEL output characteristics.

<sup>5</sup> Author to whom any correspondence should be addressed.

**Contents**

<b>1. Introduction</b>	<b>2</b>
<b>2. HHG seed sources</b>	<b>5</b>
2.1. Energy and tuning . . . . .	5
2.2. Implementation . . . . .	7
<b>3. Undulator, focusing lattice and 3D steady-state simulations</b>	<b>9</b>
3.1. Undulator module and gap length . . . . .	10
3.2. 3D steady-state simulation summary . . . . .	11
3.3. Undulator tuning . . . . .	12
<b>4. Modelling the HHG seed</b>	<b>14</b>
4.1. Seed injection . . . . .	14
4.2. Seed with full harmonic content. . . . .	15
<b>5. XUV-FEL output</b>	<b>18</b>
5.1. 100 eV photon energy simulations . . . . .	18
5.2. 10 eV photon energy simulations . . . . .	20
5.3. Variable polarisation. . . . .	22
<b>6. Seed pulse synchronisation</b>	<b>23</b>
6.1. The synchronisation system . . . . .	23
6.2. Timing offset effects. . . . .	26
<b>7. Conclusions</b>	<b>28</b>
<b>Acknowledgments</b>	<b>29</b>
<b>References</b>	<b>29</b>

**1. Introduction**

The 4th generation light source (4GLS) project is to be based at the UK's Daresbury Laboratory and consists of a suite of synchronised coherent variably polarised radiation sources covering the spectrum from THz frequencies to photon energies of  $\sim 100$  eV [1]. This facility will provide the scientific community with a tool that will enable new windows of scientific exploration to be opened and thereafter exploited. Initially, the major themes of the 4GLS science programme will lie in time-resolved measurements and nanoscience. Particular areas of strength are high resolution pump-probe spectroscopy of atoms, molecules and clusters, including high field dynamics, dynamics at surfaces and interfaces, many-body problems in condensed matter, and studies of the dynamics of biomolecules in 'real' environments. Details of the science case driving the need for 4GLS were first published in [2] and more recently updated in [1].

The 4GLS facility is planned to be a multi-source, multi-user facility. This is achieved by superconducting radio-frequency (SCRF) accelerator technology, operating using energy recovery, to provide short-pulse spontaneous radiation with pulse duration variable from ps to  $\lesssim 100$  fs. At long wavelengths significant coherent synchrotron radiation (CSR) will be generated so that 4GLS will provide enormously bright THz radiation. The high quality, low emittance electron beam provided by the photoinjectors additionally provides an ideal source with which to operate free electron lasers (FELs). In the 4GLS conceptual design these are embedded within the facility, delivering ultra-high brightness short-pulse radiation in the infra-red (IR),

vacuum ultra violet (VUV) and extreme ultra violet (XUV) energy ranges, with pulse lengths as short as  $\sim 50$  fs full width half maximum (FWHM). In world terms, this gives a unique suite of synchrotron radiation (SR) and FEL sources covering the THz to the soft x-ray range. Many of the light pulses originate from the same electron bunch, thus offering potential levels of internal synchronisation at the tens of femtoseconds level. All the 4GLS sources are offered with variable polarisation, while the flexibility of SCRF technology allows the repetition rates of the sources to be varied. The FEL sources offer a typical peak brightness enhancement of eight orders of magnitude when compared with 3rd generation light sources.

The 4GLS accelerator design concept consists of three inter-related accelerator systems [3, 4]. The high average current loop uses energy recovery as an essential element to deliver a 600 MeV electron beam of 77 pC bunches at repetition rates of up to 1.3 GHz. Distributed bunch compression allows for SR pulse lengths from a few ps to approximately 100 fs (root mean square, RMS) to be delivered according to user requirements. A low-Q cavity VUV-FEL source is incorporated at the end of this loop. The most challenging area of accelerator design for 4GLS is in transporting and accelerating an extremely high quality high-average current (100 mA) beam around this loop, while simultaneously providing high peak current (1.5 kA) at 750–950 MeV for the second accelerator system, the XUV-FEL branch. This beam is derived from 1 nC bunches produced by a normal conducting radio frequency (RF) photoinjector operating at 1 kHz and it is dumped after traversing a final spontaneous undulator source at the exhaust of the XUV-FEL. The third accelerator system is required for the IR-FEL where SCRF linac technology is used to accelerate electrons to 25–60 MeV to provide a fully integrated and synchronised IR-FEL facility.

The major 4GLS component discussed in this paper is the XUV-FEL which has already undergone several design iterations [5]–[7]. The current design is for a seeded FEL amplifier that operates in the 8–100 eV photon energy range to provide near Fourier-transform limited pulses of FWHM duration  $\sim 100$  fs at a repetition rate of  $\sim 1$  kHz and of peak powers between approximately 1–10 GW allowing high field intensities of up to  $10^{17}$  W cm $^{-2}$  to be achieved. While not reported from the simulations presented here, the transverse coherence properties of high gain FEL amplifiers are generally considered good [8]. In order to tune over the spectral range both the electron beam energy and the undulator magnetic field are variable. Because the FEL acts as an amplifier the seed sources also need to be continuously tunable.

A schematic of the XUV-FEL branch is highlighted in the schematic of the major components of the 4GLS facility in figure 1. Typical operating parameters and specification of the XUV-FEL branch are given in table 1.

There are several potential benefits in operating an FEL as an amplifier of an injected seed as opposed to allowing the FEL to self-seed from inherent noise to generate self amplified spontaneous emission (SASE). Probably the most important is the potential improvement in the temporal coherence of the FEL output over that of SASE, so increasing the spectral brightness. Shot-to-shot reproducibility and stability may also be greatly improved. If the seed power is sufficient to dominate that generated by electron shot-noise then, under correct conditions of seed/electron pulse coincidence, the injected seed will saturate before significant SASE interaction. The amplified pulse width, being determined by that of the seed, may be significantly shorter than that of the electron pulse, and indeed there is the potential to amplify more exotic pulses for post-amplification manipulation. Finally, the length of FEL interaction required to achieve saturation may be shortened, thereby reducing space requirements and ultimately costs.

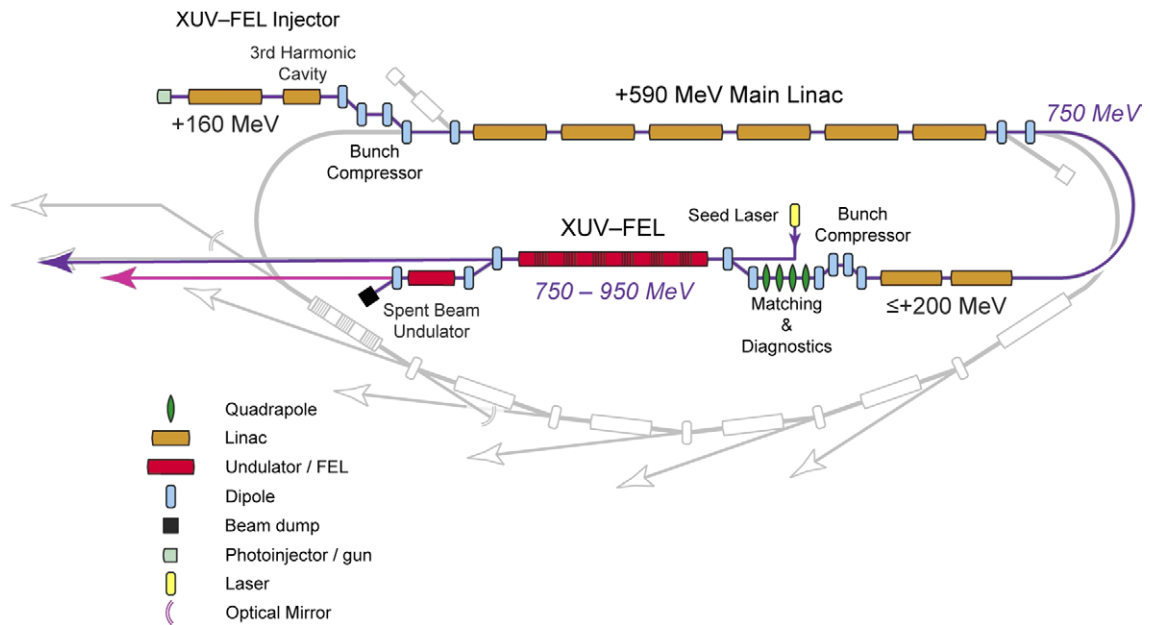


**Figure 1.** Schematic layout of the 4GLS conceptual design with the XUV-FEL branch highlighted in colour.

All of these benefits require that the seed power be significantly greater than the spontaneous power due to the inherent shot-noise.

In what follows some of the major design considerations and choices for the XUV-FEL are discussed. Given that 4GLS must operate as a user facility over extended periods as specified by its users, generating stable, synchronous and reproducible radiation pulses over the wide spectral range to end-user stations, the aim of the conceptual design of 4GLS has been to create a robust design that does not overly stress the specification of its individual components.

In section 2 the high harmonic generation (HHG) seed sources are discussed and characterised. Issues regarding their tunability and pulse energy are addressed and a design that meets the requirements of the XUV-FEL amplifier is presented.

Details of the electron beam focusing lattice, undulator tuning and three-dimensional (3D) steady-state estimates of the XUV-FEL output are given in section 3.

In section 4, injection of the HHG seed field into the FEL and the effect that the attosecond pulse structure, particular to (unfiltered) HHG sources, has on the FEL interaction are discussed.

In section 5 the results of simulations of the XUV-FEL output toward either end of its expected operational tuning range are presented. Also discussed is the contrast between the seeded to SASE output, optimal seed focusing and achieving variable polarisation in the mixed planar/variable undulator system.

Of critical importance is the synchronism in the arrival of the seed and electron bunches at the beginning of the FEL interaction region. The design of the timing system is presented and an analysis and simulations of the effects of timing offset are presented in section 6.

Conclusions and future research plans drawn from the 4GLS XUV-FEL design process are presented in section 7.

**Table 1.** XUV-FEL conceptual design parameters.

General	
FEL design	High gain amplifier
Seeding mechanism	High harmonic generation (HHG) source
Photon output	
Tuning range	$\sim 8\text{--}100$ eV
Peak power	$\sim 8\text{--}2$ GW
Repetition rate	$\sim 1$ kHz
Polarisation	Variable elliptical
Min pulse duration FWHM	$< 50$ fs
Typical $\Delta f \Delta t$	$\sim 0.6$
Max pulse energy	$400 \mu\text{J}$
Electron beam parameters	
Energy	$750\text{--}950$ MeV
Bunch charge	$1$ nC
RMS bunch duration	$266$ fs
Normalised emittance	$2 \pi$ mm mrad
RMS energy spread	$0.1\%$
Undulator parameters	
Undulator type	Pure permanent magnet (PPM) and APPLE-II
No. of modules	$8$ and $5$
Module lengths	$\sim 2$ m
Period	$45$ and $51$ mm
Focusing	FODO
Minimum magnetic gap	$\sim 10$ mm

## 2. HHG seed sources

The use of HHG [9, 10] as a seed source for FELs is currently under consideration in several proposed facilities [11]–[14]. An HHG seed will be independent of machine dynamics, and allows extensive manipulation of the seed pulse using well-established techniques of ultrafast laser physics. These allow for rapid tuning, and offer the prospect of extending FEL chirped pulse amplification and even pulse shaping for coherent control to short wavelengths. There are a number of issues important to the implementation of HHG seeding of an FEL including spectral range, tunability, coherence, temporal structure, etc. In this section these issues are discussed with respect to their application in the 4GLS XUV-FEL.

### 2.1. Energy and tuning

A number of groups have measured harmonic yields from Ti : sapphire driven systems. A synopsis of recent experimental results [15]–[17] is shown in figure 2. The results represented here (unconnected points on the plot) were obtained from experimental data which used a range of fundamental pump pulse energies from 3 to 50 mJ. The data are scaled to estimate the expected HHG energy resulting from a single fundamental pump pulse energy of 14 mJ—the energy of the Ti : sapphire system described below. Provided conditions on the focusing geometry are observed, over this energy range, the scaling of the harmonic yield will be linear in the pump

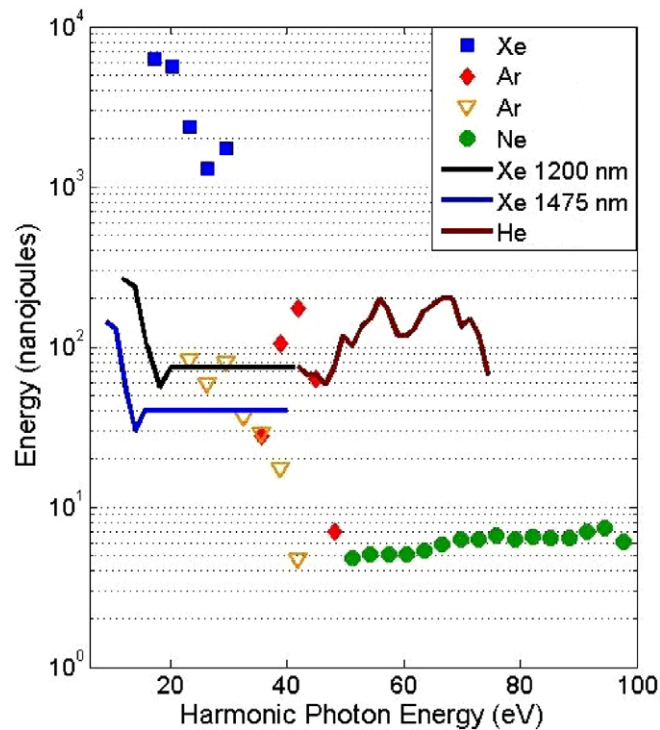


**Figure 2.** Recent HHG experimental results scaled by energy and wavelength. The unconnected points were taken with an 800 nm fundamental, and are scaled here to a fundamental pump pulse energy of 14 mJ. The solid Xe curves show the limits of the projected range of harmonic yields for the non-colinear optical parametric amplifier (NOPA) (2 mJ pulse energy), tuning between 1200 and 1475 nm. The solid He curve shows the results of a two-colour experiment using 800 and 400 nm fundamentals, scaled to a 14 mJ pump energy. The minimum energy for seeding the XUV-FEL with a 30 fs pulse is 1 nJ.

energy. This is consistent both with experimental studies of scaling over the 5–20 mJ range [15] and with the theoretical understanding of HHG yields in the loose-focusing regime [18]–[20]. These scaled yields exceed 4GLS requirements by over three orders of magnitude at the low energy end of the XUV-FEL operating range, and by a factor of six at the high energy end.

The fundamental pump pulse energy of 14 mJ was chosen because such a laser system has been demonstrated to operate at the kHz repetition rates [21] required for the XUV-FEL. This is therefore a conservative estimate of the energy that will be available, as ultrafast laser technology is developing very rapidly, and extension to higher powers is not constrained by any fundamental limit. A number of recent developments, e.g. the use of optical parametric chirped pulse amplification [22], high power Yb:YAG lasers [23], and enhancement cavities [24]–[26], offer new opportunities for more powerful longer wavelength systems. Several 100 W kHz system designs have been proposed [27], and are expected to be demonstrated in the near future. Considerable effort by the HHG community is also being focused on extending the wavelength range and yield of harmonics. Recent experiments [17] using two-colour fields demonstrated an enhancement of over two orders of magnitude in the harmonic yield in helium to produce 150 nJ at the 38th harmonic (59 eV), using only 2.8 mJ in the pump laser. Figure 2

shows the results of that experiment (scaled from the experimental energy of 2.8 mJ to 14 mJ). Since helium is the least efficient of the rare gas targets used, it is reasonable to expect that when these techniques are extended to other gases and longer pump wavelengths, seed energies across the XUV-FEL operating range will increase substantially over those currently available.

The simplest and most versatile way to tune between the harmonic orders is through control of the amplitude and phase of the fundamental pump. Methods can be as simple as a chirp [28]–[30], but more general adaptive pulse shaping [31]–[34] allows a greater tuning range and a greater control over the harmonic pulse width to be achieved. This latter method presents minimal impact on synchronisation during tuning, and is rapid once the system has been calibrated. The tuning range is of the order of  $q\Delta\nu$ , where  $q$  is the harmonic order and  $\Delta\nu$  is the bandwidth of the fundamental. Thus, this method does not work well for low harmonic orders. Reitze *et al* [32] have demonstrated complete tunability (i.e. a tuning range exceeding the separation of adjacent harmonics) down to 40 eV in Argon using 28 fs, 800 nm pulses, a tuning range of  $2.2q\Delta\nu$ . For an energy below 40 eV, complete tunability will be lost. For this reason, a tunable fundamental is proposed for seeding the XUV-FEL for photon energy operation below 40 eV.

Using a tunable fundamental, however, entails a double loss: from the frequency conversion losses of the pump and a reduced harmonic efficiency at longer pump wavelengths [35]. Conversion to wavelengths shorter than 800 nm, where the harmonic efficiency is higher, is possible, but then the harmonic orders used to reach the very low end of the tuning range are smaller, and complete tunability cannot be obtained. For an infrared source tunable from 1200 to 1475 nm, complete tunability would be obtained. Conversion efficiencies for commercial non-collinear phase-matched optical parametric amplifier (NOPA) systems in this range, pumped by a Ti : sapphire system, are typically 10%, while laboratory systems have reported efficiencies of 20% [36]. The efficiency of harmonic generation  $\propto 1/\lambda^3$  [35, 37, 38], where  $\lambda$  is the pump wavelength, so that, over the NOPA tuning range, the harmonic efficiency is 15–30% of that obtained at 800 nm. Nevertheless, harmonic generation efficiencies are still high enough at these lower harmonics to generate sufficient seed power. Figure 2 shows the projected range of the tunable source's harmonic yields in xenon using the expected wavelength scaling of the harmonic efficiency, and assuming 15% conversion efficiency in the NOPA. Above 40 eV, tuning is achieved using adaptive control of the Ti : sapphire fundamental.

Developments in laser technology will probably make this two-track system unnecessary in the near future, as new high-power kilohertz ultrafast sources in the 1–2  $\mu\text{m}$  wavelength range are developed [27]. Because the high energy cutoff of harmonic generation increases as  $\lambda^2$  at longer wavelengths [39], gases with higher harmonic efficiency can be used to generate higher photon energies, offsetting some of the wavelength-dependent reduction in efficiency. A longer fundamental wavelength also increases the wavelength range over which adaptive tuning may be used, since the harmonic order  $q$  for a given wavelength increases and the harmonic spacing decreases. For example, assuming an adaptive tuning range of  $2q\Delta\nu$ , a source with a fixed wavelength of 1.8  $\mu\text{m}$  and 20 fs pulse width could cover the entire XUV-FEL photon energy range using only adaptive tuning.

## 2.2. Implementation

The current design for implementing HHG seeding in the 4GLS XUV-FEL is shown schematically in figure 3. An ultrafast Ti : sapphire oscillator producing 30 fs, 800 nm pulses is synchronised at a subharmonic of the accelerator RF frequency. Pulses are selected at 1 kHz

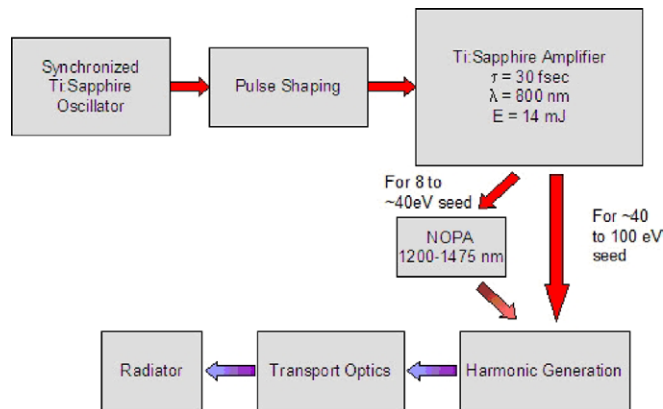


**Figure 3.** Block diagram of HHG seeding system for the 4GLS XUV-FEL.

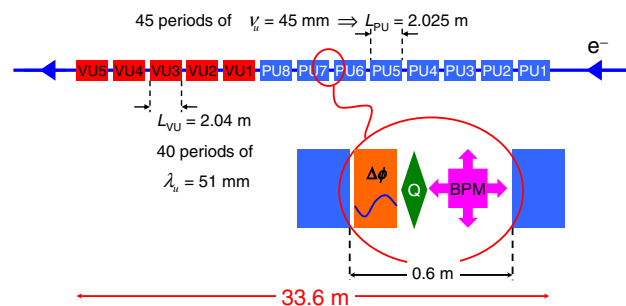


**Figure 4.** Schematic of the modular undulator system of the XUV-FEL. Undulator modules PU1..8 (blue) are planar undulators; VU1..5 (red) are variable polarisation undulators. The gap between undulator sections may contain a beam position monitor, quadrupole and radiation/electron phase matching unit.

and amplified to 14 mJ. Amplifier chains capable of this power presently exist [21], and systems with higher output are expected to appear soon. After amplification, the pulse is switched into one of two paths, depending on the FEL photon energy. For low energies (8 to approximately 40 eV), a tunable pump pulse is generated using a NOPA operating between 1200 and 1475 nm. At higher energies (40–100 eV), the 800 nm light is used for HHG, and adaptive tuning is used. Pulse shaping for the adaptive tuning can be done either before the amplifier, as shown here, or afterward. The geometry for the HHG is still under study. A loose focusing geometry in a variable length cell is the simplest to implement over the entire range of the XUV-FEL and is equivalent to waveguide geometries at sufficiently high power [19]. Waveguide geometries [40] may be beneficial for the low photon energies, where the pump pulse energy is lower. Modulated waveguide geometries [41] may provide greater efficiency, but it may be difficult to implement multiple configurations to cover the entire wavelength range. Efficient materials (e.g. SiC) for grazing incidence optics are available for the optics coupling the HHG seed into the undulator.

### 3. Undulator, focusing lattice and 3D steady-state simulations

The design for the XUV-FEL undulator consists of a lattice of undulator modules containing both planar and variable polarisation undulator modules. For the planar undulators a relatively simple PPM was chosen and an APPLE-II design was chosen for the variable polarisation undulators. Each type of module will have a fixed period and a variable magnetic gap,  $g$ , that allows tuning of the RMS undulator parameter  $\bar{a}_u$  via the undulator magnetic field. A minimum undulator magnetic gap is assumed for the design of both planar and variable undulators. Note that the gap between the vacuum vessel walls will be  $(g - 3)$  mm, the 3 mm reduction from the magnetic gap being the estimated thickness of the vacuum vessel walls and the clearance between magnets and vacuum vessel. A schematic giving further detail of the undulator lattice and incorporating beam positioning monitors, phase matching devices and the focusing quadrupoles is shown in figure 4. The variable polarisation undulator sections, VU1..VU5, ensure that variably polarised photons may be generated across the full design spectrum. In practice, operation at higher photon energies will require a longer undulator length to achieve saturation. The effective undulator length may be varied by opening the magnetic gaps of individual undulator modules to their maximum. Those modules that have maximum magnetic gap generate only small on-axis magnetic fields and are effectively switched off for the purpose of the FEL interaction. For example, when operating for 100 eV photon energy generation all undulator modules PU1..VU5 would be functional to achieve saturation, whereas for 50 eV operation only modules PU5..VU5 would need to be functional to achieve saturation, with PU1..PU4 gaps fully opened. This method of operation should allow a tapered vacuum vessel to be used along the undulator modules which will assist with reducing diffraction effects of HHG seed injection at lower photon energies as discussed in section 4. The minimum undulator parameter due to undulator gap tuning is taken to be  $\bar{a}_u \approx 1$  to ensure sufficient FEL coupling. With this constraint then for a beam energy of 950 MeV the maximum planar undulator period that can achieve 100 eV FEL resonance is  $\lambda_u \approx 45$  mm with a gap of  $g \approx 28$  mm. At the lower beam energy of 750 MeV and for  $\lambda_u \approx 45$  mm, the resonant photon energy is  $\approx 10$  eV for the minimum magnetic gap of  $g \approx 10$  mm. The period of  $\lambda_u \approx 45$  mm is then the optimum for the beam energy, magnetic gap and photon tuning range. A similar analysis for the variable polarisation APPLE-II undulators gives them an optimum period  $\lambda_u \approx 51$  mm.

A FODO focusing lattice has been chosen for the conceptual design. Other systems based upon quadrupole doublet and triplet focusing were investigated [6] and rejected. Although these latter designs allow longer, and therefore fewer, undulator modules of up to 4–5 m in length to be used, the quadrupole field strengths must be significantly greater by a factor of 3–4 than those required for a FODO lattice distributed between more modules. Tighter quadrupole alignment tolerances would therefore be required for the doublet and triplet positioning [42]. Monitoring of the electron beam transverse position, critical to the FEL interaction, would also be limited as would the ability to step-vary the full undulator length by opening the individual module gaps. For these reasons a simpler FODO focusing lattice of module length  $\approx 2$  m is the chosen design option.

In order to investigate the effect of  $\beta$ -function variation due to the discrete focusing quadrupoles of the FODO lattice, the 3D code Genesis 1.3 [43] was used to determine both the saturation length  $L_{\text{sat}}$  and power  $P_{\text{sat}}$  as a function of average  $\beta$ -function. This was carried out for a planar undulator system of module length  $\approx 2$  m. The respective results are shown in figure 5. It is seen that  $\beta \approx 3.5$  m minimises the saturation length whereas  $\beta \approx 5.5$  m maximises the output

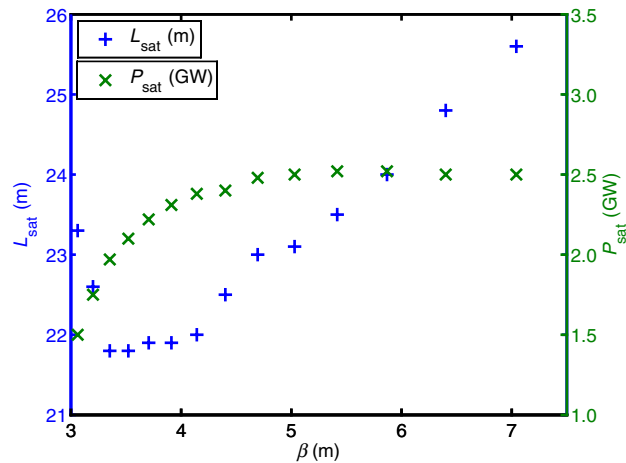


**Figure 5.** Genesis simulation of the saturation length,  $L_{\text{sat}}$ , and power,  $P_{\text{sat}}$ , as a function of the  $\beta$ -function in a FODO lattice for 100 eV operation.

power. The nominal value of the  $\beta$ -function is chosen to be that which gives the maximum output power :  $\beta = 5.5$  m. This is motivated by the fact that the planar modules PU1–PU8 produce a seed pulse (and pre-bunched beam) which will be amplified to saturation in the APPLE-II modules VU1..VU5, so maximising the power of the seed into the VU modules reduces the required length of the more technologically challenging APPLE-II modules. For the parameters used here a  $\beta$ -function of 5.5 m is satisfied by quadrupoles of magnetic length 0.09 m and of strength  $13 \text{ T m}^{-1}$ . The RMS electron beam radius may be calculated as  $\sigma_b = \sqrt{\epsilon_n \beta / \gamma} = 77 \mu\text{m}$  for beam energy 950 MeV and the design normalised emittance  $\epsilon_n = 2 \text{ mm mrad}$ .

### 3.1. Undulator module and gap length

The modular construction of the combined undulator and FODO focusing lattice requires choice of the length of each undulator module,  $L_{\text{PU}}$  for planar and  $L_{\text{VU}}$  for variable undulators, and  $L_{\text{gap}}$  the spacing between modules. The FEL performance has a functional dependence on these parameters so optimisation is needed. The energy dispersion induced into the electron beam by the FEL interaction, and the natural homogeneous energy spread, are transformed into a spatial dispersion in proportion to the gap between undulator sections,  $L_{\text{gap}}$  which may disrupt the FEL bunching process. Furthermore, it is seen from figure 4 that the undulator module length and gap define the FODO focussing lattice period,  $\lambda_{\text{FODO}} = 2(L_{\text{PU}} + L_{\text{gap}})$ . In a FODO lattice, the  $\beta$ -function varies about its mean value by  $\pm \lambda_{\text{FODO}}/2$  so affecting the electron beam radius via the relation above for  $\sigma_b$ . Thus if  $\lambda_{\text{FODO}}$  is too large (as determined principally by the module length) the electron beam radius variation may also adversely affect the FEL coupling. Variation in the  $\beta$ -function due to larger values of  $\lambda_{\text{FODO}}$  also causes de-phasing of the electrons which can inhibit the electron bunching process [44, 45]. This may also be a factor contributing the reduced coupling. We have not attempted here to disentangle the two effects but simply note the results from simulation.

Alignment of the electron beam through the undulators is of critical importance to maintain the electron–radiation coupling. This requires both beam alignment between undulator modules and careful construction of the undulators to ensure that the beam wander due to magnetic field

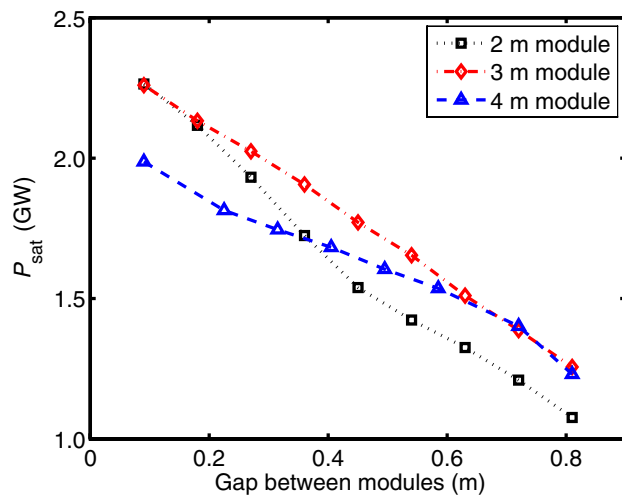


**Figure 6.** Simulation of the saturation power,  $P_{\text{sat}}$ , for XUV-FEL planar undulator operation at 100 eV as a function of the gap between undulator modules. The results are plotted for three module lengths :  $L_{\text{PU}} = 2, 3$  and 4 m.

errors and pole alignment are minimised. Ideally, beam wander off the optical axis should be no greater than 20% of the electron/radiation beam radius [46].

Genesis 3D simulations were carried out to simulate the FEL operating at 100 eV. Only the planar undulator modules were used with the nominal design parameters. Figure 6 plots the results of Genesis steady-state simulations for the saturation power,  $P_{\text{sat}}$ , as a function of the gap between undulator modules,  $L_{\text{gap}}$ , for three different module lengths,  $L_{\text{PU}}$ . It is seen that the saturation power is nearly independent of the undulator module length and decreases almost linearly with the undulator gap. A gap of  $L_{\text{gap}} = 0.6$  m is chosen for the design specification. This is the estimated minimum length into which the quadrupoles, BPMs and phase matching units can fit.

Simulations of the saturation length  $L_{\text{sat}}$  of a seeded amplifier interaction, starting from a seed power of 30 kW at 100 eV, are shown in figure 7. For each length of undulator module  $L_{\text{sat}}$  is seen to increase with the module gap. However, there is a significant difference between each undulator module length, with the 4 m module having a saturation length longer than that of the 2 m module. This is attributed to the greater variation in the  $\beta$ -function for the longer module as discussed above. For this reason, and the greater opportunities for beam monitoring and control afforded by the greater number of undulator modules, the module lengths for the design specification are chosen to be  $L_{\text{VU}} \approx L_{\text{PU}} \approx 2$  m. Hence, for the baseline design for 8–100 eV operation, each planar PPM undulator will have 45 periods of 45 mm giving a module length  $L_{\text{PU}} = 2.025$  m and each variable undulator APPLE-II undulator will have 40 periods of 51 mm giving a length  $L_{\text{VU}} = 2.04$  m.

### 3.2. 3D steady-state simulation summary

The design choices and optimisations discussed may be summarised by plotting both the saturation powers and lengths across the operating spectrum of the XUV-FEL. It has been

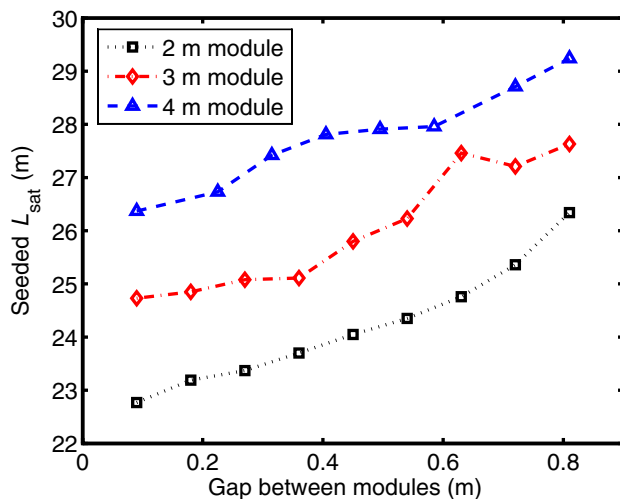


**Figure 7.** Simulation of the saturation length  $L_{sat}$  for XUV-FEL planar undulator operation at 100 eV as a function of the undulator module gap,  $L_{gap}$  for three module lengths :  $L_{PU} = 2, 3$  and 4 m. (The saturation length is the undulator length only : gaps between modules are not included.)

assumed that the XUV-FEL is operating in an amplifier mode with a seed power  $\sim 10\%$  of the peak power currently available from seed pulses as described in section 2. The reduction in seed power by a factor of approximately ten conservatively estimates the power available following transmission and focusing losses from the seed laser into the undulator. The seed is focused to the centre of the first in-use undulator module with Rayleigh length equal to half the module length. Seed pulses of 30 fs FWHM and of energy 3 nJ for 10–40 eV photons and 1 nJ for 40–100 eV, give approximate peak powers of 100 and 30 kW respectively. The saturation power over the operational spectral range as calculated by both Genesis (in steady-state mode) and Xie formulae [47] are shown in figure 8. Both planar and helical mode results are shown. Note that the Xie design formulae cannot take into account mixed planar/helical undulators, so the ‘Xie helical’ estimates assume a helical-only undulator for the equivalent length of the planar-helical combination. The Xie estimates also do not include the effects of gaps between undulator modules. These differences account for the small discrepancy of the ‘Xie helical’ estimates from the other simulations, in the slightly higher saturation power estimation. Notwithstanding this, the 3D numerical and Xie estimates are in excellent agreement. In figure 9, the length of undulator required for saturation is plotted as a function of photon energy. Note that the gaps between undulator modules are not included in this length and must be added on to obtain the total length of the combined undulator-focusing lattice.

### 3.3. Undulator tuning

A schematic for the undulator/focusing lattice is shown in figure 10. Also shown are the injected radiation seed fields focused to the beginning of the first resonant undulator module, for each of the cases. The undulator length is therefore controlled so that saturation always occurs in the final variable undulator module VU5. In this way, variable polarised photons may be generated

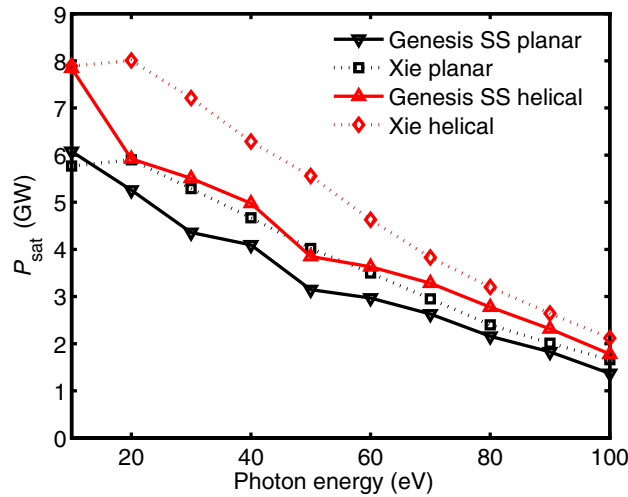


**Figure 8.** Summary of saturation power estimates for the XUV-FEL across its spectral operating range. 3D Genesis steady-state (SS) simulations and the Xie formulae are in excellent agreement.

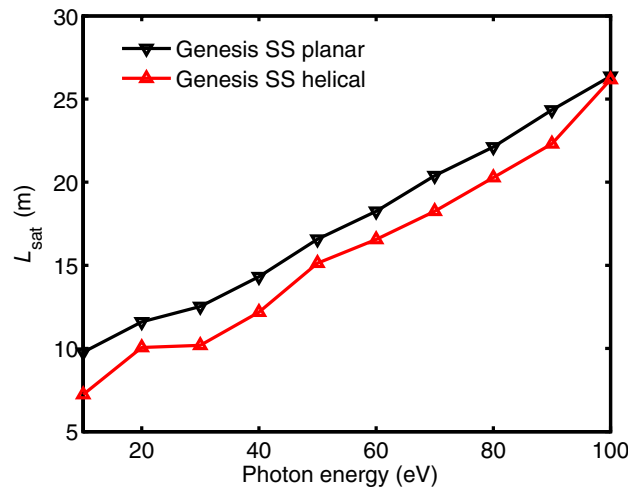


**Figure 9.** Summary of steady-state 3D Genesis simulation estimates for the XUV-FEL undulator saturation length across the spectral operating range.

across the full operational range of the FEL and it acts as a fixed source simplifying the optical transport system of the output to the experimental areas.

It can be seen from figure 10 that planar undulator module PU1 is only required to ensure saturation at  $\sim 100$  eV and that its magnetic gap will be at the operational maximum of  $\sim 28$  mm. This module will not be required to operate at gaps very much smaller than this, and therefore the vacuum vessel aperture containing both electron beam and radiation seed can be relatively large at this point. Similar considerations show that module PU2 will operate with minimum magnetic gap slightly smaller again, and so on for the rest of the modules PU3..PU8. Use of



**Figure 10.** Schematic of the modular undulator system and focusing lattice of the XUV-FEL demonstrating the different modes of operation across the photon energy range 10–100 eV. Electron beam transport and seed injection is right to left with increasing  $z$ . Undulator modules marked in grey have large magnetic gaps  $\bar{a}_u \approx 0$  and are effectively absent for the purposes of the FEL interaction. The minimum required undulator gap (and vacuum vessel internal aperture) decrease in gradual steps from 28 mm (25 mm) for PU1 down to 10 mm (7 mm) for PU8 and the variable polarisation modules VU1..VU5. Radiation beam waists of the seed and output are shown from 100 eV (violet) to 10 eV (red).

a step-tapered vacuum vessel has therefore been proposed that gradually decreases in aperture from module to module. The two advantages of this approach are that firstly resistive wall and surface roughness wakefields are much reduced compared to a constant minimum aperture, and secondly, as discussed in section 4, the tapered internal aperture allows optimal focusing of the seed pulse across the whole wavelength range. Preliminary investigation of wakefield effects using the Genwake package of Genesis has shown that, even with a constant minimum aperture of  $\sim 8$  mm along the full length of the undulator system, wakefield effects have only a small effect on both saturation length and power across 10–100 eV operation. These wakefield effects will be studied in more detail in future work.

## 4. Modelling the HHG seed

### 4.1. Seed injection

For effective seeding, the seed pulse should be injected coincident with the electron pulse at the start of the first operational undulator module and focused to a waist,  $w_0$ , of approximately the same transverse dimensions as the electron pulse. (The waist minimum  $w_0$  is defined as the radius at which the radiation power is  $1/e^2$  of its peak value.) Focusing should not be so tight that the seed diffracts rapidly within a gain length at the start of the FEL interaction (i.e. when the Rayleigh length  $Z_R = \pi w_0^2/\lambda \ll L_g$ ). The relation for the radiation waist size

$$w(z) = w_0 \sqrt{1 + \left( \frac{z - z_0}{Z_R} \right)^2},$$

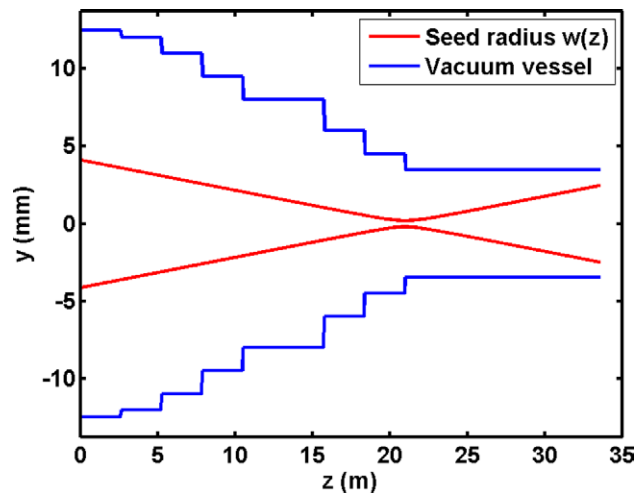


**Figure 11.** Plot of the dimension of the inner vacuum vessel wall (blue) which has been step-tapered to enable the undulator module tuning ranges of figure 10. The waist size  $w(z)$  (red) for a 10 eV seed is also shown, focused at the entrance to VU1 at  $z = 21$  m.

where  $z_0$  is the position of the focus along the axis of the undulator lattice, restricts the minimum aperture size of the vacuum vessel that will allow transmission of the seed to its focus. As the focal size is determined by the electron beam radius, which is nearly constant for all seed wavelengths, the vacuum vessel's minimum transverse dimensions are determined by the longest wavelength seed (10 eV photons) which must be focused furthest from the FEL entrance as shown in figure 10. As the minimum operational undulator gap decreases with undulator module PU1..PU8, as discussed for figure 10, the vacuum vessel may be tapered to accommodate the focusing of the 10 eV photon energy seed. This is demonstrated in figure 11, where the seed field is injected at the entrance of undulator module PU1 and focused to the optimal waist (as shown in following simulations) of  $w_0 = 200 \mu\text{m}$  at the entrance of module VU1 approximately 21 m downstream. It is seen that the vacuum vessel inner wall dimension at  $z = 0$  is 25 mm to accommodate wall thickness and clearance for the 28 mm undulator magnetic gap. The walls are at least two beam waists away from the peak power on axis at all positions up to the start of the FEL interaction region at  $z \approx 21$  m. Thus the tapered vacuum vessel should provide sufficient clearance for injection of this (worst case) 10 eV seed injection.

#### 4.2. Seed with full harmonic content

The method of seed generation and specification across the XUV-FEL spectral range is summarised in the previous section and described in more detail in [1, 48]. The HHG seed has interesting spectral and temporal properties, being composed of a large number of narrow, phase-coherent odd harmonics of a fundamental drive laser. This forms a comb structure in frequency-space. Such a phase correlated comb in frequency space has a similar comb-like structure in the temporal domain, resulting in a series of attosecond pulse structures each separated by one half the drive laser period. For a drive laser such as the Ti : sapphire laser with wavelength of  $\sim 800$  nm, the 65th harmonic corresponds to the maximum XUV-FEL photon energy of 100 eV. If the complete frequency content of a HHG pulse were to be injected into the XUV-FEL it

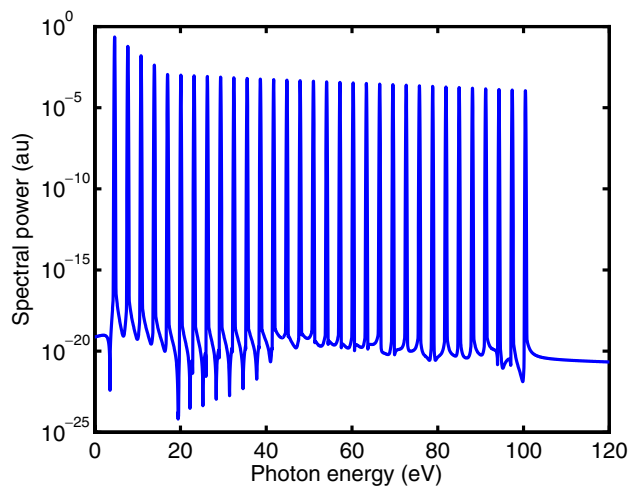


**Figure 12.** Simulated power spectrum from an HHG source.

would be preferable if only one of the harmonics, say the  $n$ th harmonic, interacts resonantly with the electrons. The half width half maximum (HWHM) gain bandwidth  $\Delta\lambda/\lambda \approx \rho$ , where  $\rho$  is the FEL parameter [49], should then be less than the spacing between harmonics. This gives the condition  $\rho < 1/n$ . A typical value of  $\rho \approx 2\text{--}3 \times 10^{-3}$  for 100 eV operation so that  $\rho < 1/65 \approx 1.5 \times 10^{-2}$  is easily satisfied. Thus, it should be possible to inject all of the seed radiation, including all non-resonant harmonics, into the XUV-FEL without the need for band-pass pre-filtering of the seed, as all non-resonant harmonics will simply become negligible relative to the resonant harmonic as the FEL interaction proceeds through the undulator. For the purposes of investigating these effects a typical HHG radiation field was generated for use with the 3D code Genesis. The full HHG spectral power is shown in figure 12. However, Genesis is a time-averaged code with a minimum interval between sample points of the field of one radiation period so the sampling rate is  $\Delta t_s = f_r^{-1}$ , the inverse of the resonant frequency. The Nyquist frequency,  $f_N = 1/2\Delta t_s$ , determines the bandwidth of frequencies that the field can contain without the effects of aliasing. Hence the range of frequencies that can be simulated by Genesis without aliasing effects is  $f_r/2 < f_r < 3f_r/2$ . Thus from figure 12 it is seen that if simulating 100 eV photon energy generation in the XUV-FEL, only the 50–100 eV components of the HHG spectrum should contribute to the Genesis input file using its ‘RADFILE’ option.

A Genesis simulation was performed for 100 eV operation with the limited spectral range HHG seed pulse as described above. A uniform current of 1.5 kA was assumed. Due to the relatively short slippage experienced at these photon energies, this is very close to that experienced by a short pulse coincident with the Gaussian peak current of the XUV-FEL. All 13 undulator modules were assumed to be the planar type modules PU1..8. The seed at the beginning of the FEL interaction at  $z = 0$ , the entrance to PU1, is plotted in figure 13. Here, the parameter  $s$  is the distance as measured from ‘tail’ of the electron bunch. Both the attosecond structure in the pulse power and the comb of odd-harmonic wavelengths (inset) are clearly visible. The peak power of the resonant 100 eV ( $\sim 12.3$  nm) component is approximately 22 kW. On propagating through the amplifier to  $z = 16.2$  m, figure 14 shows that the fine attosecond structure is beginning to be ‘washed out’ due to the selective amplification of the resonant wavelength at 12.3 nm (inset). All non-resonant harmonics of the seed appear unaffected by the resonant FEL interaction. This

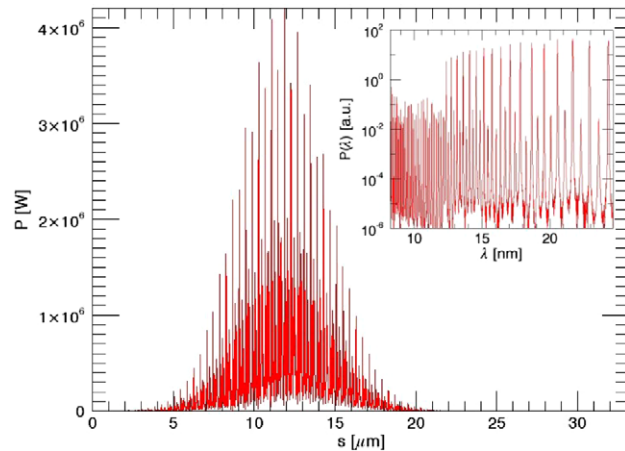


**Figure 13.** Radiation seed power at the beginning of the amplifier  $z = 0$  m as a function of local distance,  $s$ . The spectral power content of this pulse is shown as a function of radiation wavelength in the inset.

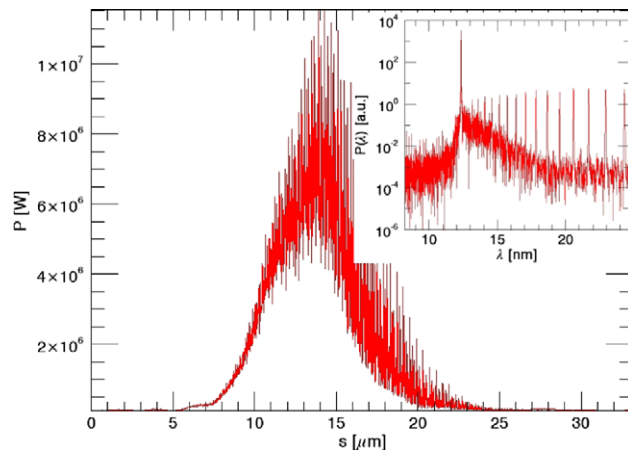


**Figure 14.** Radiation power as a function of local distance,  $s$ , at  $z = 16.2$  m through the amplifier. The spectral power content of this pulse is shown as a function of radiation wavelength in the inset.

is further confirmed by figure 15 which shows the output at saturation at  $z = 32.4$  m, the end of the interaction region. The radiation pulse shows none of the attosecond structure of the input seed and the spectral power density shows a single high power emission at the resonant wavelength 12.3 nm.

Although a simplified phase relationship among the harmonics has been assumed [50] and geometric effects are ignored in this model, the extreme contrast in the output spectrum indicates that a physical picture of out-of-resonance harmonics in the seed simply undergoing free-space propagation, without gain, is essentially correct, and that these details may be neglected. It is concluded that, at least for these 3D simulations, the injection of the (Nyquist limited) harmonic content of the HHG seed appears to have no adverse effects in the FEL evolution, or in the saturated emission. The same conclusion may be drawn for lower photon energy XUV-FEL operation where the condition to enable neglect of non-resonant HHG content,  $\rho < 1/n$ , is more

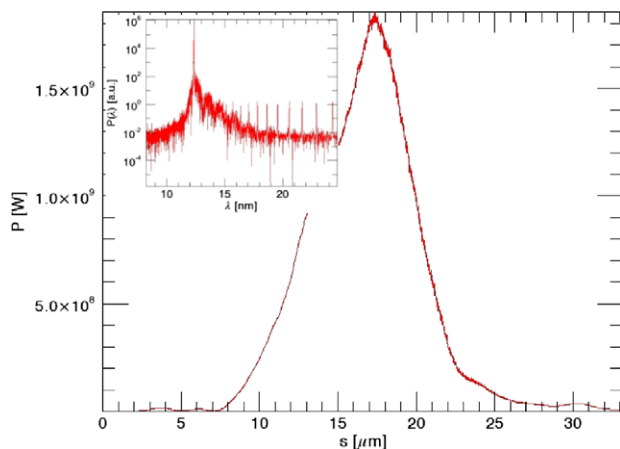


**Figure 15.** Radiation power as a function of local distance,  $s$ , at the end of the amplifier,  $z = 32.4$  m. The spectral power content of this pulse is shown as a function of radiation wavelength in the inset.

easily satisfied. Thus in all subsequent simulations only the resonant harmonic of the HHG seed content is used in the simulation input.

## 5. XUV-FEL output

### 5.1. 100 eV photon energy simulations

A complete simulation of the design for the XUV-FEL operating at 100 eV is now demonstrated, using the parameters as given in table 1. Full details of all parameters may be obtained in [1]. The system modelled is that of figure 10 which, for 100 eV operation, uses the full set of planar and variable undulator modules with the FODO lattice incorporated between modules. The variable APPLE-II undulator modules VU1..5 are set to helical mode so that circularly polarised radiation is generated. The radiation power is plotted in a spatial window that travels along the undulator axis at the speed of light. Figure 16 plots the power distribution of the seed pulse of peak power  $P_{\text{pk}} = 30$  kW and duration 30 fs FWHM at the entrance to the first undulator section, PU1. The seed is assumed to have only the resonant harmonic component so that none of the atto-second structure discussed above is present. Also plotted is the electron beam current, here assumed Gaussian, of peak current  $I_{\text{pk}} = 1.5$  kA and duration 626 fs FWHM. At the exit of the planar undulator modules, it can be seen from figure 17 that the peak radiation power has increased to  $\approx 70$  MW with little change in the pulse structure or width. This pulse and the co-propagating electrons are then injected into the set of APPLE-II undulators, VU1 to VU5. By the end of this set of undulator modules, it is seen from figure 18 that the FEL interaction has saturated, achieving a peak power of  $P_{\text{pk}} \approx 2.5$  GW and of duration  $\Delta t \approx 60$  fs FWHM. Fourier analysis gives the bandwidth of the spectrum as  $\Delta\nu/\nu \approx 5.6 \times 10^{-4}$  which gives a time-bandwidth product of  $\Delta f \Delta t \approx 0.8$  which compares favourably with that for a transform limited Gaussian pulse of  $\Delta f \Delta t \approx 0.44$ . A log plot of the same data clearly shows in figure 19 the relatively clean central seeded region upon a noisier pedestal. This pedestal is the amplified SASE radiation which remains well below saturation because of the smaller initial spontaneous noise radiation

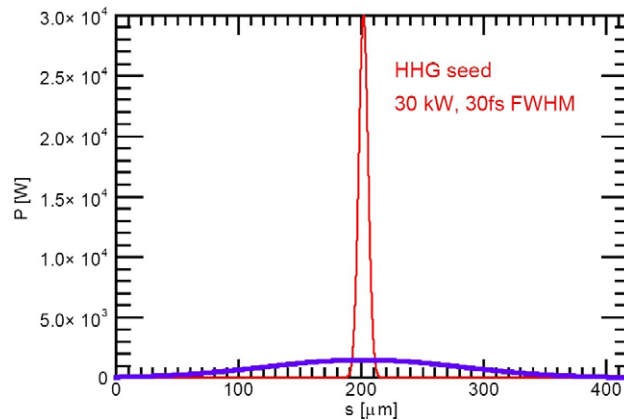


**Figure 16.** Input radiation seed power (red) to PU1 as a function of local distance,  $s$ . The electron beam current profile (blue) is also shown against the same numerical scale.

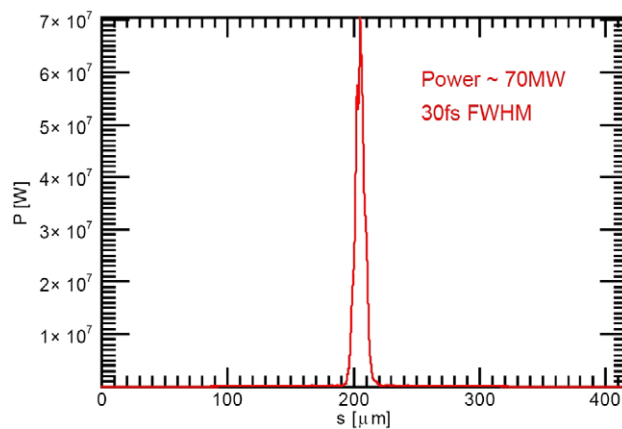


**Figure 17.** The radiation power at the exit of PU8 as a function of local distance,  $s$ .

(typically a few tens of watts), compared with the initial peak seed power of 30 kW. The shape of the saturated pulse power envelope is not quite as Gaussian as may be expected which suggests that the FEL interaction may have progressed just past saturation. Taking the output power at the end of the previous undulator module, VU4, and plotting it in a similar log plot in figure 20, a cleaner Gaussian shape can be seen, with a slightly reduced peak power of  $P_{\text{pk}} \lesssim 2 \text{ GW}$ . The improved pulse shape is confirmed from the pulse duration of  $\Delta t \approx 43 \text{ fs}$  FWHM and spectral bandwidth of  $\Delta\nu/\nu \approx 6 \times 10^{-4}$  giving an improved time–bandwidth product of  $\Delta f \Delta t \approx 0.63$ . An improved contrast between the peak power and that of the SASE pedestal is also evident.

In general, for all operational photon energy ranges of the XUV-FEL, the saturation length will be decreased by increasing seed power. The contrast ratio between the peak power and the SASE pedestal power at saturation should vary approximately linearly with the seed power.

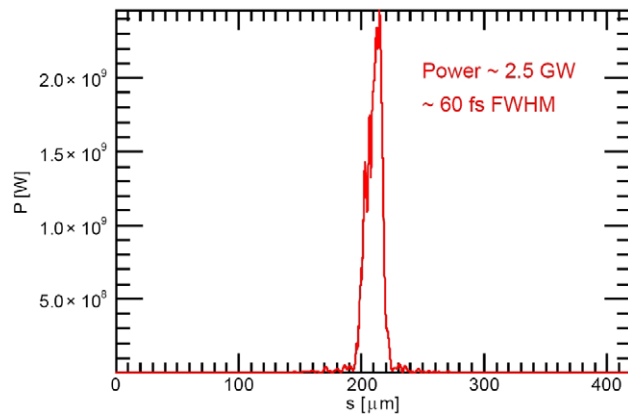


**Figure 18.** The radiation power at the exit of VU5 as a function of local distance,  $s$ .

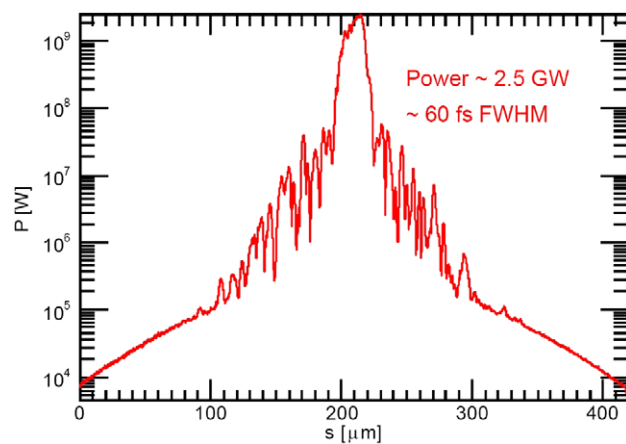


**Figure 19.** A log plot of the radiation power at the exit of VU5 as a function of local distance,  $s$ .

### 5.2. 10 eV photon energy simulations

Similar simulations to those at 100 eV were carried out for the case of 10 eV operation of the XUV-FEL. Now only the APPLE-II undulator modules VU1 to VU5 are required to achieve saturation as shown schematically in figure 10. The input seed power is Gaussian with a peak power  $P_{\text{pk}} = 100 \text{ kW}$  and duration 30 fs FWHM. The electron pulse current will have the same Gaussian distribution as that for the 100 eV case of figure 16.

Radiation power output at the end of undulator module VU5 is shown in figure 21 using a log scale. Pulse quality is very good with a peak power of  $\approx 6 \text{ GW}$  and pulse time–bandwidth product very close to that of a transform-limited Gaussian ( $\Delta t \Delta f \approx 0.44$ ). If the radiation is instead extracted at the end of undulator VU4, the radiation power output is shown in figure 22.

A better contrast between the peak power of  $P_{\text{pk}} \approx 1 \text{ GW}$  and the SASE pedestal power is seen from the case of figure 21, indicating that the FEL had already saturated before the end of VU5. The time–bandwidth product is approximately the same at  $\Delta t \Delta f \approx 0.48$ .

Time-dependent Genesis 1.3 simulations have also been used to assess the sensitivity of the XUV-FEL output power to the seeding geometry. It is assumed that the most difficult photon

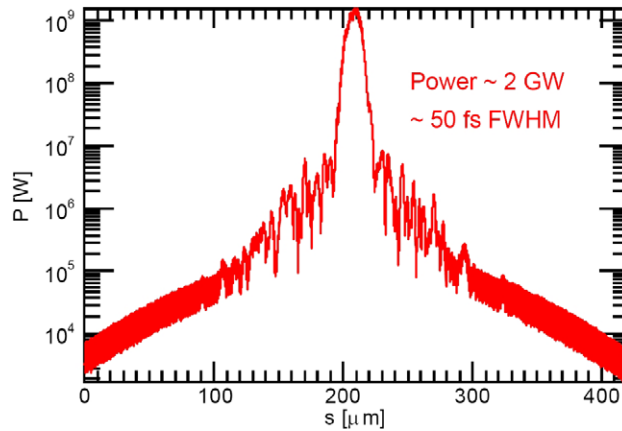


**Figure 20.** A log plot of the radiation power at the exit of VU4 as a function of local distance,  $s$ .

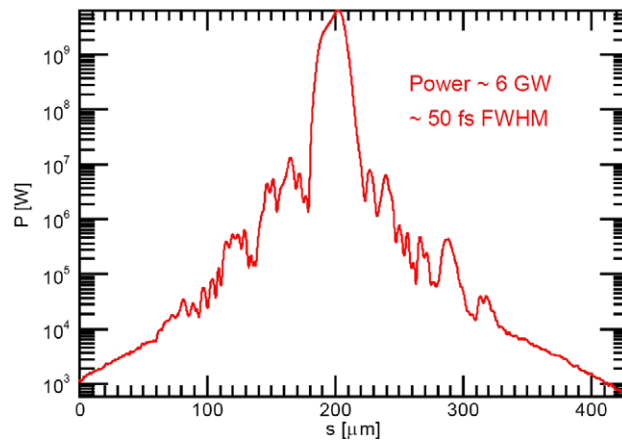


**Figure 21.** Log plot of the radiation power for 10 eV operation at the end of undulator module VU5, as a function of local distance,  $s$ .

energy to achieve optimum geometry will be 10 eV because of the relatively long distance of  $\approx 21$  m between the seed injection point (before PU1) and the first operational undulator (VU1). The peak seed power of 100 kW was focused to a waist at the beginning of VU1. Figure 23 shows the effect of varying the size of the focal point waist. An optimum waist of  $\approx 200 \mu\text{m}$  yields a peak output power of  $P_{\text{pk}} \approx 7.5$  GW. The corresponding Rayleigh length for this focus is  $\approx 1.0$  m. The Xie formulae [47] estimates the gain length at 10 eV for these parameters to be  $\approx 0.5$  m. The optimum Rayleigh length for a seed focused at the undulator entrance is therefore found to be  $Z_{\text{R opt}} \approx 2L_{\text{g}}$ . For this optimum focusing the seed beam waist radius at the injection point,  $z = 0$  (beginning of PU1), is 4.1 mm. If it is assumed that a full aperture at the injection point of six times the beam radius is required to minimise diffraction effects, then a vacuum vessel aperture of  $\approx 25$  mm (magnetic gap minus 3 mm) is sufficient. This is achieved with the step-tapered vacuum vessel design, as discussed above.

The above results show that the output power at the end of VU5 reduces as the seed waist size at the entrance to VU1 increases. (Consequently the seed radius at the injection point also decreases.) The reduced coupling between radiation and electrons with increasing radiation

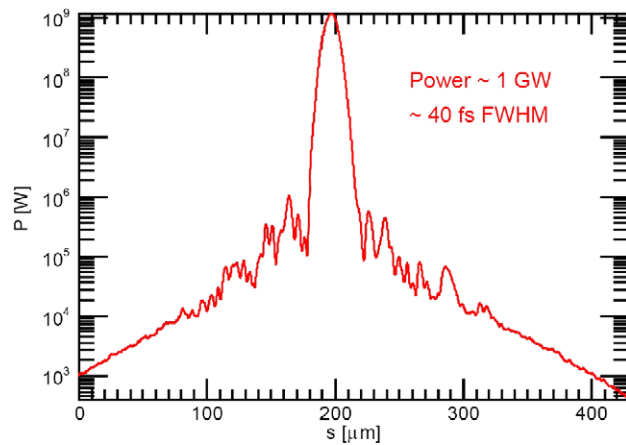


**Figure 22.** Log plot of the radiation power for 10 eV operation at the end of undulator module VU4, as a function of local distance,  $s$ .

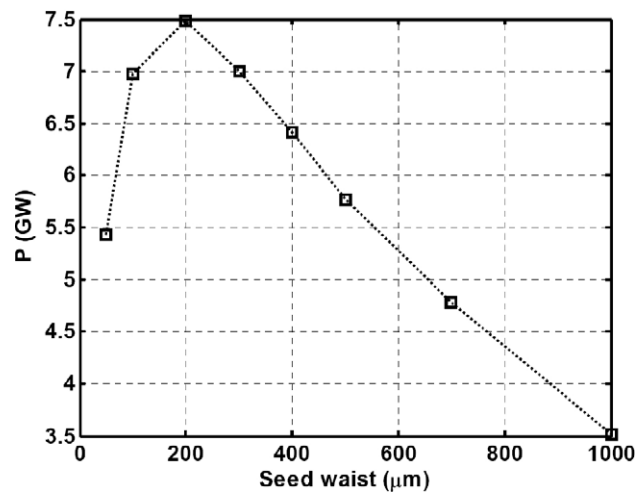


**Figure 23.** Radiation peak power for 10 eV operation at the end of undulator module VU5, as a function of seed beam waist at the entrance to VU1.

waist means that saturation is not achieved in the fixed undulator length. Nevertheless, it may be beneficial to use a larger seed waist size than the optimum value of  $200 \mu\text{m}$  and compensate for the increased saturation length by focusing the seed into the previous module PU8 for example. (This will have no effect on the saturation power which is independent of seed.) A larger waist size will reduce output power fluctuation due to seed source pointing stability. While this will be investigated further in future design work, the current conclusion shows that the optimum seed focusing geometry may be obtained with the use of the proposed step-tapered vacuum vessel.

### 5.3. Variable polarisation

As has been noted above, the HHG seed sources are linearly polarised. However, this should not present problems in generating variable polarisation. When the HHG seed is injected into a planar undulator it causes the electrons to bunch in the axial ( $\hat{z}$ ) direction. The polarisation of the radiation emitted is determined by the electron trajectory. Hence, if the electron bunching is

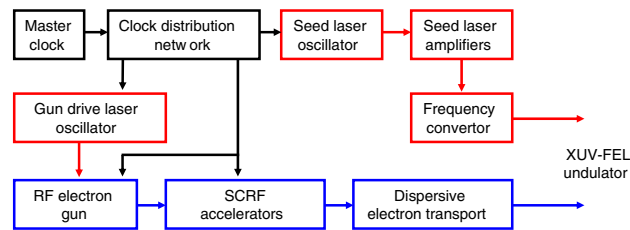


**Figure 24.** Layout of the XUV-FEL synchronisation system showing photon generation and transport (red) and electron generation and transport (blue).

initiated in a planar undulator and subsequently transferred into an elliptically polarised undulator, the electrons will emit elliptically polarised radiation and progress via the FEL interaction to saturation. If the linearly polarised HHG seed is injected with the electrons directly into an elliptically polarised undulator then coupling between seed and electrons will occur in the plane of the radiation electric field and will begin to bunch the electrons. The bunched electrons will then emit with the elliptical polarisation determined by the undulator. Optimal coupling will occur when the major axis of the elliptically polarised undulator is co-incident with that of the electric field polarisation of the seed.

## 6. Seed pulse synchronisation

Of critical importance to any seeded FEL is the correct timing of the seed pulses and the electron bunches to ensure their coincidence at the start of the FEL interaction region. Other aspects of 4GLS, such as pump–probe synchronisation, have many similar requirements for tight timing control, so a distributed synchronisation system covering the whole facility is proposed. For the XUV-FEL, where a Gaussian electron current distribution of duration 626 fs FWHM is assumed, it is desirable to lock the seed pulse and electron bunches together with a jitter  $\lesssim 50$  fs as discussed in section 6.2. This is a challenging target for a system tens of metres in size and which contains many distinct elements. In this section the proposed synchronisation system is described and the effects of timing jitter on the FEL interaction are modelled.

### 6.1. The synchronisation system

A schematic of the XUV-FEL section of the synchronisation system is shown in figure 24. Trigger signals from a master clock are sent via a distribution network to the two laser oscillators at the start of the seed pulse and electron bunch transport chains. The seed and electrons follow distinct paths to the FEL undulator passing through laser amplifiers and frequency converters in the case of the seed and RF accelerators (also phase-locked to the master clock) and bunch compressors in the case of the electrons. All of these elements can, in principle, influence the seed and electron arrival times.

Since all the controlled elements of the system are phase-locked to the master clock, phase noise in the clock itself will only matter on timescales comparable with the elements' response times. The slowest elements are the SCRF cavities, whose extremely high  $Q$  means that their electromagnetic RF fields take milliseconds to respond. It is important that the master clock timing remains steady over this period to avoid timing shifts between the SCRF and faster-responding elements (e.g. the laser oscillators, which may track clock noise up to 1 kHz).

The clock will consist of an ultra-low noise fibre laser oscillator phase-locked, at low frequencies, to a state of the art 1.3 GHz RF source. A similar system has demonstrated timing jitter of  $\sim 50$  fs between 100 Hz and 1 kHz [51], much of which arose from the inherent noise of the RF source. With a more stable source the 100 Hz–1 kHz noise should be reducible to 20 fs or less. The timing of the seed is set by its generating laser oscillator and the length of the optical path to the FEL. The Ti : sapphire oscillator has been described above in section 2. Such lasers have, in optimised circumstances, been locked to external clocks with less than 2 fs jitter [52]. More realistically, locking at the 20 fs level has been sustained for long periods in a practical user environment [53]. This will be the initial target figure for the XUV-FEL seed oscillator. The clock signal will be subject to jitter generated during its distribution. This can be minimised by using a distribution system based on short laser pulses transported on optical fibres. Schemes have been developed for active stabilisation of the fibre lengths and for low jitter optical to electrical conversion to regenerate the RF. The resulting jitter can be as low as 15 fs (the quadrature sum of 12 fs from the fibre [54] and 9 fs from the optical to electrical converter [55]). The 4GLS system will be designed to deliver at least this performance.

Once the seed pulses have been generated they must pass through the laser amplifier chain and either one (harmonic) or two (OPO plus harmonic) nonlinear frequency conversion stages before being transported to the FEL. The nonlinear processes are simply parametric and do not contribute significantly to the timing jitter. The imaginary component of the refractive index which corresponds to the optical gain in the laser amplifiers has an associated real component which affects the optical path length and hence the timing of the optical pulses. However, this index component is small and the diode pumped solid state lasers used to pump modern Ti : sapphire systems are very stable, so any timing jitter arising from laser amplification should be negligible. The physical length of the transport path from the laser oscillator to the FEL will be relatively long. In particular the laser pulses will circulate 20 to 30 times in the optical cavity of the regenerative amplifier, travelling many tens of metres in the process. Stable pulse timing requires good positional stability of all of the beam transport mirrors and good control of any media through which the beam passes. The use of optical interferometry over distances up to 10 m is routine in the optical fabrication industry, demonstrating that path length stability can be achieved at the level of one part in  $10^8$ . Provided that the same degree of care is taken with opto mechanical hardware and environmental control (in particular of vibration and temperature) it should be possible to maintain the same fractional stability over longer path lengths. Timing fluctuations of less than 5 fs should thus be achievable over a 100 m (330 ns) path.

The arrival time of the electron bunches at the FEL is affected by several factors. The most important of these is the combination of off-crest acceleration and dispersive beam transport which is used to compress the RMS bunch duration from  $\sim 5$  ps after the photo-gun to  $\sim 266$  fs at the FEL [1]. The system is complex, with four independent RF-powered elements (controllable in both amplitude and phase, measured relative to the electron gun timing) and four dispersive sections. This system's overall behaviour can only be determined accurately by detailed simulation. The results which follow are based on a preliminary numerical model designed to optimise the electron bunch current profile at the undulator.

The compression scheme takes electron bunches which start with a relatively long bunch duration and delivers them to the FEL with a significantly shorter duration. A side effect is the reduction of any timing jitter which the electron bunch might have as it leaves the photo-gun. Provided this is not much larger than the initial electron bunch duration it will be reduced

by approximately the same factor as the bunch duration, i.e. by approximately 50 times. The photo-gun drive laser will consist of a fibre oscillator followed by a conventional amplifier. The oscillator will be phase-locked directly to the distributed clock signal. Such locking has been demonstrated with less than 10 fs jitter [56]. Combining this with the clock distribution jitter (12 fs) and the amplification and transport jitter (5 fs) the overall jitter of the photo-gun drive laser is expected to be  $\sim 17$  fs. The compression scheme should reduce the direct impact of this to the sub-femtosecond level.

It might seem that this jitter reduction removes the need for tight timing control on the gun drive laser, but because the XUV-FEL uses an RF gun any laser mis-timing will also affect the electron energy distribution. This will, in turn, affect the electron bunch arrival time at the entrance to the FEL undulator. The model predicts an arrival time sensitivity to energy at the photo-gun exit of  $6.4 \text{ fs kV}^{-1}$ , so that an energy jitter of  $\sim 150 \text{ eV}$  would generate an arrival time jitter of 1 fs. With a nominal output energy of 4 MeV the photo-gun could operate at up to  $15^\circ$  off crest before its drive laser timing jitter of 17 fs generates a 150 eV energy jitter. In practice the photo-gun will not be operated this far off crest, so its drive laser timing jitter will again have negligible effect on the bunch arrival time.

A 1D model has been used to track the electrons from the output of the photo-gun through the accelerating and dispersive sections. It allows the dependence of the bunch arrival time on the individual RF phases and amplitudes to be determined. Assuming that the RF noise is uncorrelated between individual elements the overall noise sensitivities can be estimated by combining individual contributions in quadrature. The bunch arrival time dependence for the RF phase was found to be  $3.1 \text{ ps deg}^{-1}$ . The preliminary specification for RF phase stability on 4GLS is  $0.01^\circ$  yielding a corresponding 31 fs timing jitter which is acceptably low, being below the target 50 fs overall value given above. However, the model predicts an overall timing sensitivity to percentage RF amplitude noise of  $14.5 \text{ ps}/\%$ . It has been proposed to maintain RF amplitude noise below 0.01% but at this level the resulting timing jitter would be  $\sim 145$  fs which is a factor 3 greater than the target. Methods to reduce this RF amplitude noise-induced jitter are discussed below.

The electron bunch arrival times at the FEL will vary if the physical positions of the beam transport magnets change (e.g. because of mechanical vibration or thermal expansion), or if the strength of their fields changes (e.g. due to power supply fluctuations). Assessing the impact of magnet effects requires a detailed knowledge of the 4GLS lattice design which has not yet been finalised. So, although this contribution to the timing jitter may be significant it will not be discussed here further.

Table 2 summarises the jitter contributions for the various XUV-FEL synchronisation sub-systems. Assuming that these contributions are uncorrelated their combined total is 152 fs. At this level the seed photons and the electron bunch would be timed within the target 50 fs on fewer than 30% of the machine's shots.

As discussed above, the greatest contribution to the jitter total arises from the effect of RF amplitude fluctuations. If this can be reduced to the same level as the RF phase contribution then the total would very nearly meet the target at 55 fs. The first approach to reducing the jitter should be a re-optimisation of the machine operating point. Sensitivity to RF amplitude may be traded off against phase sensitivity, final energy spread of the electron bunch and field in the SCRF cavities (since higher fields allow operation further from crest).

If the jitter cannot be reduced to an acceptable level by resetting the operating point then more active solutions will be required. One option would be to sense the arrival time of the

**Table 2.** Contributions to the timing jitter (fs RMS) between seed photon pulses and electron bunches at the entrance to the XUV-FEL undulator.

Source	Timing jitter
Master clock (100 Hz–1 kHz)	20
Signal distribution to seed laser oscillator	15
Seed laser oscillator	20
Seed laser amplifier and photon beam transport	5
Electron gun drive laser	< 1
RF phase in accelerator cavities	31
RF amplitude in accelerator cavities	145
Total (assuming contributions are uncorrelated)	152

electron bunches directly and use this signal to drive a feedback control system acting on the RF field in the accelerating cavities. This should stabilise the electron arrival time to a level set by the sensor resolution, by noise arising in the control loop and by the RF driver response. An electron sensor with a timing resolution of 30 fs and with the potential for further improvements has recently been reported [57]. The 1 kHz bunch rate at the XUV-FEL undulator would set a Nyquist upper limit of 500 Hz on the noise which could be sensed but, as noted above, this is expected to be well above the upper limit of the noise due to SCRF field fluctuations. An additional possibility would be to lock the seed laser oscillator to the output of the electron timing sensor instead of to the master clock. This would eliminate most of the effects of electron timing jitter and should ensure good overlap between the seed photons and the XUV-FEL electron bunches. The disadvantage would be that the XUV-FEL output would no longer be locked through the master clock to all of the other 4GLS sources.

Of course, the jitter target of  $\lesssim 50$  fs may be reduced if a flatter, non-Gaussian current profile can be generated. For the case of the BESSY FEL their modelling predicts electron bunches with an almost ‘flat-top’ current of 2 kA of length 730 fs [58]. In this case an acceptable temporal jitter would be slightly less than half of this value considerably relaxing the 4GLS design target of  $\lesssim 50$  fs. The combined jitter estimate of 152 fs above would therefore easily satisfy the jitter tolerances for a BESSY-type electron bunch.

### 6.2. Timing offset effects

The jitter tolerance target of  $\lesssim 50$  fs is an estimate based on the assumption of a Gaussian electron bunch current profile of length 626 fs FWHM and which ensures that the power output from the XUV-FEL will be within  $\sim 90\%$  of the peak power generated for perfect electron bunch/seed pulse synchronism [1, 59]. While the assumption of a Gaussian electron bunch current makes this a demanding target, it provides a realistic margin of safety before detailed simulations have been performed.

Genesis simulations have been used in section 6.2.1 to investigate the effect of timing offset upon the power of the XUV-FEL operating at 100 eV and are in reasonable agreement with the Xie estimates of section 6.2.2. However, for the case of a jitter estimate of  $\sim 150$  fs as calculated from section 6.1, the Genesis simulations predict a variation in output power of up to  $\sim 50\%$ .

A simple relation between the timing offset  $\Delta t$  and the peak electron current [59] has been used with the Xie formulae [47] in section 6.2.2 to estimate the effects of timing offset

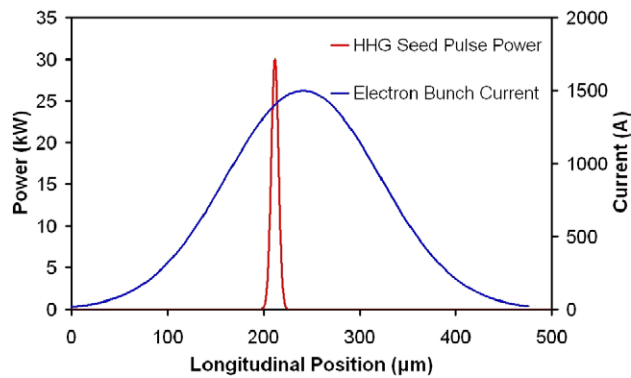


**Figure 25.** Seed offset by 100 fs ( $30 \mu\text{m}$ ) behind the electron pulse.

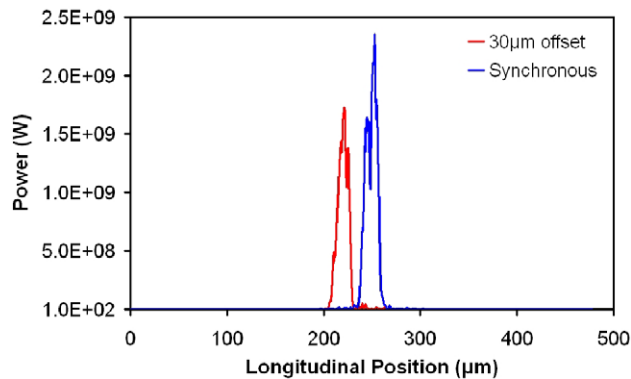


**Figure 26.** Radiation power at the end of the FEL for the  $\Delta t = 100$  fs offset case (red) and synchronous case (blue).

upon the saturation length in addition to the saturation power. From these estimates a 50 fs offset increases the saturation length by  $\sim 1.3\%$ , and decreases the saturation power by  $\sim 4\%$ . A 100 fs offset increases the saturation length by  $\sim 5\%$ , and decreases the saturation power by  $\sim 13\%$ .

In addition to the compensating effects of a flat-top current as discussed above, it may also be possible to compensate for jitter effects by adding extra length to the undulator. While this will mean that for perfect electron/seed synchronism the output may be oversaturated, in those instances where jitter introduces a timing offset, the extra length should be sufficient to achieve saturated output. This is partially supported by the results presented in section 5.1 and is the subject of ongoing research effort.

**6.2.1. 100 eV pulse amplifier lasing with offset seed.** Genesis simulations have been carried out in which the offset  $\Delta t$  is varied for 4GLS XUV-FEL operation at a photon energy of 100 eV. The effect of a timing offset of  $\Delta t = 100$  fs between the seed pulse and the electron bunch current is shown in figure 25.

In figure 26 the radiation power at the end of the FEL, with the synchronous seed case plotted for comparison, shows that for seed offset of  $\Delta t = 100$  fs, the peak power is reduced from 2.4 to 1.7 GW.

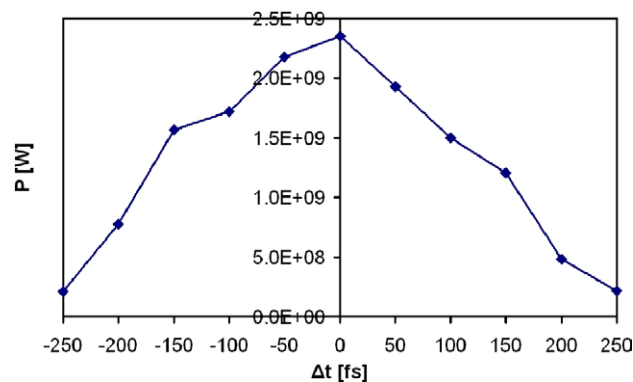


**Figure 27.** The effect of an offset  $\Delta t$  from electron/seed pulse synchronism upon the output power  $P$  at the end of the FEL, for 100 eV operation.

Genesis simulations were also carried out for variation in the offset between  $\pm 250$  fs and the power  $P$  is plotted as a function of offset in figure 27. For the Gaussian current case considered here the results suggest that electron bunch jitter should be limited to approximately  $\pm 45$  fs for peak output power to lie within 90% of the synchronous peak power  $P_{pk}$ . It is noted from figure 27 that the output power at the end of the FEL is higher for a negative  $\Delta t$  (seed pulse arriving after the electron bunch) than for a positive offset of the same magnitude. This is because the seed pulse for a negative offset  $\Delta t$  propagates into an increasing electron current due to the relative electron/radiation slippage, whereas for a positive offset the radiation propagates into a decreasing electron current.

*6.2.2. Comparison with FEL design formulae.* The Xie design formulae [47] have also been used to estimate the effects of timing offset on the radiation output power for 100 eV operation. This was done by correlating the timing offset  $\Delta t$  with the Gaussian form of the electron pulse current. In figure 28 these Xie estimates are compared with those of the Genesis simulations by plotting the output powers expressed as a fraction of the power at synchronism,  $\Delta t$ . Both Xie and Genesis output was taken at the end of the planar undulator section PU8 of figure 10. The interaction had therefore not yet achieved saturation and explains the small discrepancies with figure 27. The Genesis simulations are seen to yield slightly more stringent restrictions on  $\Delta t$ . Nevertheless, the results are in reasonable agreement.

## 7. Conclusions

The main use of HHG in 4GLS is to act as a seed source for the XUV-FEL. These sources have enabled a robust conceptual design for the XUV-FEL to be developed. Established theory and simulation codes predict that this FEL will generate photons of giga-watt power levels in pulses of length 40–60 fs FWHM. The design specification presented here is optimised for 10–100 eV operation but it has been demonstrated [1] that extension to a revised photon energy limit of 8 eV requires only small parameter changes. The quality and tunability of the HHG seed ensures the FEL remains continuously tunable generating pulses that will have very good temporal and spatial coherence with time–bandwidth products close to the Fourier-transform

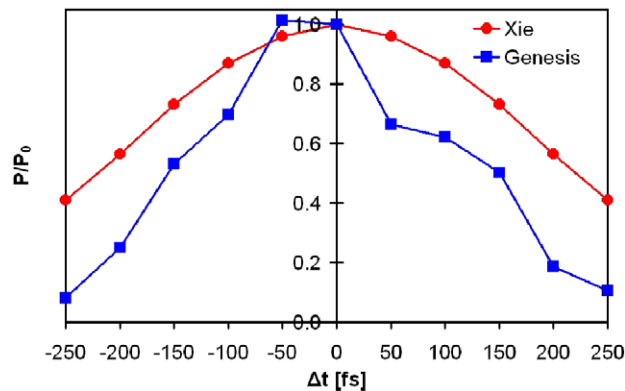


**Figure 28.** Simulations of the effect of a timing offset  $\delta t$  from electron/seed pulse synchronism upon the fractional output power with respect to its synchronous value.

limit for a Gaussian pulse. The XUV-FEL interaction here is acting as a simple, bandwidth limited amplifier—so long as the radiation input seed pulses have sufficient spectral purity, the output radiation is very nearly a simple amplified version of the input.

HHG sources have also been included in the 4GLS conceptual design as user sources in their own right. This has not been discussed, but is of significant importance to the overall concept of 4GLS as a facility providing multi-colour synchronised sources to the user.

It has been demonstrated that the multi-harmonic content of the HHG seed need not be filtered before injection as the gain-bandwidth of the FEL interaction ensures that only the resonant harmonic affects the FEL output.

The most critical aspect to ensuring the success of the XUV-FEL design is in the spatio-temporal synchronisation between electron pulses and HHG seed at the beginning of the FEL interaction region. The initial study suggests a total jitter estimate of  $\sim 150$  fs and that this will result in output pulse power fluctuations of  $\sim 50\%$ . This figure should be considered a worst case scenario that can be improved upon by utilising methods such as active feedback control and electron bunch shaping to give more flat-top electron bunches that are less sensitive to timing jitter than the Gaussian pulses used here. These factors give optimism that the power fluctuations predicted here may be reduced significantly and this will be the subject of further research.

## Acknowledgments

This work has been supported in part by the EU Commission in the Sixth Framework Program, contract no. 011935-EUROFEL. We are grateful for helpful discussions with Steven Jamison, Elaine Seddon, Wendy Flavell and Mike Poole.

## References

- [1] CCLRC 2006 *4GLS Conceptual Design Report* Council for the Central Laboratory of the Research Councils (UK) online at <http://www.4gls.ac.uk/documents.htm#CDR>
- [2] CCLRC 2006 *The Science Case for 4GLS* Council for the Central Laboratory of the Research Councils (UK) online at [http://www.4gls.ac.uk/Documents/EP SRC-Dec2001/Science\\_Case.pdf](http://www.4gls.ac.uk/Documents/EP SRC-Dec2001/Science_Case.pdf)

- [3] Poole M W and Seddon E A 2005 *Proc. 2005 Particle Accelerator Conf. (Knoxville, TN)* pp 431–3 Joint Accelerator Conferences Website, <http://www.jacow.org>
- [4] Clarke J A 2006 *Proc. EPAC 2006 (Edinburgh)* pp 181–3 Joint Accelerator Conferences Website, <http://www.jacow.org>
- [5] Poole M W and McNeil B W J 2003 *Nucl. Instrum. Methods Phys. Res. A* **507** 489
- [6] McNeil B W J, Robb G R M, Thompson N R, Jones J, Poole M W and Gerth C K M 2005 *Proc. 27th Int. Free Electron Laser Conf. (Stanford)* pp 506–9 Joint Accelerator Conferences Website, <http://www.jacow.org>
- [7] McNeil B W J, Thompson N R and Sheehy B 2006 *Proc. 28th Int. Free Electron Laser Conf. (Berlin)* pp 63–6 Joint Accelerator Conferences Website, <http://www.jacow.org>
- [8] Ischebeck R *et al* 2004 *Proc. EPAC 2004 (Lucerne)* pp 2580–2 Joint Accelerator Conferences Website, <http://www.jacow.org>
- [9] McPherson A *et al* 1987 *J. Opt. Soc. Am. B* **4** 595
- [10] Ferray M *et al* 1988 *J. Phys. B: At. Mol. Opt. Phys.* **21** 131
- [11] Lambert G *et al* 2006 *Proc. EPAC 2006 (Edinburgh)* pp 44–6 Joint Accelerator Conferences Website, <http://www.jacow.org>
- [12] Goldammer K, Abo-Bakr M, Follath R and Meseck A 2005 *Proc. 27th Int. Free Electron Laser Conf. (Stanford)* pp 23–6 Joint Accelerator Conferences Website, <http://www.jacow.org>
- [13] Bruni C *et al* 2006 *Proc. EPAC 2006 (Edinburgh)* pp 53–5 Joint Accelerator Conferences Website, <http://www.jacow.org>
- [14] Alesini D *et al* 2005 *Proc. 27th Int. Free Electron Laser Conf. (Stanford)* pp 491–4 Joint Accelerator Conferences Website, <http://www.jacow.org>
- [15] Takahashi E J *et al* 2004 *IEEE J. Sel. Topics Quantum Electron.* **10** 1315
- [16] Hergott J F *et al* 2002 *Phys. Rev. A* **66** 021801
- [17] Kim I J *et al* 2005 *Phys. Rev. Lett.* **94** 243901
- [18] Takahashi E J *et al* 2005 *Phys. Rev. A* **66** 021802
- [19] Kazamias S *et al* 2003 *Phys. Rev. Lett.* **90** 193901
- [20] Constant E *et al* 1999 *Phys. Rev. Lett.* **82** 1668
- [21] Nabekawa Y *et al* 1998 *Opt. Lett.* **23** 1384
- [22] Dubietis A *et al* 1992 *Opt. Commun.* **88** 437
- [23] Ripin D J *et al* 2005 *IEEE J. Quantum Electron.* **41** 1274
- [24] Jones R and Ye J 2002 *Opt. Lett.* **27** 1848
- [25] Jones R and Ye J 2004 *Opt. Lett.* **29** 2812
- [26] Ilday F Ö and Kärtner F X 2005 *Joint Conf. on Ultrafast Optics V and Applications of High Field and Short Wavelength Sources XI (Nara, Japan)*
- [27] Kärtner F X *et al* 2004 *ICFA Beam Dynamics Mini Workshop (Future Light Source Working Group) MIT Workshop on the Physics of Seeded FELs (Boston, MA)*
- [28] Zhou J *et al* 1996 *Phys. Rev. Lett.* **76** 752
- [29] Lee D G *et al* 2001 *Phys. Rev. Lett.* **87** 243902
- [30] Kim H T *et al* 2001 *Phys. Rev. A* **67** 051801
- [31] Bartels R *et al* 2000 *Nature* **406** 164
- [32] Reitze D H *et al* 2004 *Opt. Lett.* **29** 86
- [33] Pfeifer T *et al* 2005 *Opt. Lett.* **30** 1497
- [34] Pfeifer T *et al* 2005 *Appl. Phys. B* **80** 277
- [35] Lewenstein M *et al* 1994 *Phys. Rev. A* **49** 2117
- [36] Yakovlev V, Kohler B and Wilson K 1994 *Opt. Lett.* **19** 2000
- [37] Shan B and Chang Z 2002 *Phys. Rev. A* **65** 011804
- [38] Gordon A and Kärtner F X 2005 *Opt. Express* **13** 2941
- [39] Krause J L, Schafer K J and Kulander K C 1992 *Phys. Rev. Lett.* **68** 3535
- [40] Durfee C G III *et al* 1999 *Phys. Rev. Lett.* **83** 2187

- [41] Paul A *et al* 2003 *Nature* **421** 51
- [42] Faatz B and Pflüger J 2001 *Nucl. Instrum. Methods Phys. Res. A* **475** 603
- [43] Reiche S 1990 *Nucl. Instrum. Methods Phys. Res. A* **429** 243
- [44] Fawley W M, Prosnitz D and Scharlemann E T 1984 *Phys. Rev. A* **30** 2472
- [45] Bonifacio R, De Salvo Souza L and McNeil B W J 1992 *Opt. Commun.* **93** 179
- [46] Faatz B, Pflüger J and Nikitina Y M 1997 *Nucl. Instrum. Methods Phys. Res. A* **393** 380
- [47] Xie M 1996 *Proc. 1995 Particle Accelerator Conf. (Dallas, TX)* pp 183–5 Joint Accelerator Conferences Website, <http://www.jacow.org>
- [48] Sheehy B, Clarke J A, Dunning D J, Thompson N R and McNeil B W J 2006 *Proc. 28th Int. Free Electron Laser Conf. (Berlin)* pp 198–201 Joint Accelerator Conferences Website, <http://www.jacow.org>
- [49] Bonifacio R, Pellegrini C and Narducci L 1984 *Opt. Commun.* **50** 373
- [50] Antoine P *et al* 1997 *Phys. Rev. A* **56** 4960
- [51] Data extracted from Winter A, Schlarb H and Ilday F O 2006 *37th ICFA Advanced Beam Dynamics Workshop FLS2006 (Hamburg)* WG5 04
- [52] Shelton R K *et al* 2002 *Opt. Lett.* **27** 312
- [53] Jones D J *et al* 2002 *Rev. Sci. Instrum.* **73** 2843
- [54] Winter A *et al* 2005 *Proc. 27th Int. Free Electron Laser Conf. (Stanford)* pp 676–81 Joint Accelerator Conferences Website, <http://www.jacow.org>
- [55] Kim J W *et al* 2006 *Proc. CLEO/QELS 2006 (Baltimore, MD)* CTuP5
- [56] Hudson D D *et al* 2005 *Opt. Lett.* **30** 2948
- [57] Hacker K, Loehl F and Schlarb H 2006 *Proc. EPAC 2006 (Edinburgh)* pp 1043–5 Joint Accelerator Conferences Website, <http://www.jacow.org>
- [58] Meseck A 2006 *Proc. 28th Int. Free Electron Laser Conf. (Berlin)* pp 226–32 Joint Accelerator Conferences Website, <http://www.jacow.org>
- [59] Dunning D J, Thompson N R, Clarke J A, Scott D J and McNeil B W J 2006 *Proc. 28th Int. Free Electron Laser Conf. (Berlin)* pp 462–5 Joint Accelerator Conferences Website, <http://www.jacow.org>